Chin. J. Mech. Eng. (2017) 30:1032–1043
DOI 10.1007/s10033-017-0146-9

ORIGINAL ARTICLE

Multi-Field Analysis and Experimental Verification on Piezoelectric Valve-Less Pumps Actuated by Centrifugal Force

Yu-Ting Ma[1] · Zhi-Guo Pei[1] · Zhong-Xiang Chen[1]

Received: 20 November 2015 / Revised: 10 April 2017 / Accepted: 20 April 2017 / Published online: 23 May 2017

Abstract A piezoelectric centrifugal pump was developed previously to overcome the low frequency responses of piezoelectric pumps with check valves and liquid reflux of conventional valveless piezoelectric pumps. However, the electro-mechanical-fluidic analysis on this pump has not been done. Therefore, multi-field analysis and experimental verification on piezoelectrically actuated centrifugal valveless pumps are conducted for liquid transport applications. The valveless pump consists of two piezoelectric sheets and a metal tube with piezoelectric elements pushing the metal tube to swing at the first bending resonant frequency. The centrifugal force generated by the swinging motion will force the liquid out of the metal tube. The governing equations for the solid and fluid domains are established, and the coupling relations of the mechanical, electrical and fluid fields are described. The bending resonant frequency and bending mode in solid domain are discussed, and the liquid flow rate, velocity profile, and gauge pressure are investigated in fluid domain. The working frequency and flow rate concerning different components sizes are analyzed and verified through experiments to guide the pump design. A fabricated prototype with an outer diameter of 2.2 mm and a length of 80 mm produced the largest flow rate of 13.8 mL/min at backpressure of 0.8 kPa with driving voltage of 80 Vpp. By solving the electro-mechanical-fluidic coupling problem, the model developed can provide theoretical guidance on the optimization of centrifugal valveless pump characters.

Keywords Valveless pump · Centrifugal force · Piezoelectric pump · Multi-field analysis

1 Introduction

Micropumps play a key role in micro-electromechanical systems (MEMS), particularly in transportation of microfluid in fields of biopharmaceuticals, chemical analysis, medical instruments, and electro-mechanical devices [1–3]. Many types of micropumps have been developed to meet different requirements with crucial concerns of flow rate, backpressure, and accuracy for dispensing fluid. Among them, piezoelectric actuation presents great performance with advantageous features of great integration capacity, low power consumption, high efficiency, and high speed responses [4–6].

According to different working principles, piezoelectric micropumps can be classified into diaphragm pumps with check valves, valveless diaphragm pumps, peristaltic pumps and traveling wave pumps. Diaphragm pump with check valves, firstly introduced by Vanlintel, et al [7], changes volume of pump chamber by piezoelectric actuator, and uses check valves to regulate flow direction. Valveless diaphragm pump, proposed by Stemme [8], implements special ports like diffuser and nozzle elements to rectify flowing owing to different pressure drops across the ports in changed flow directions. Peristaltic pump, presented by Smith [9], uses multi-phase actuation of an array of piezoelectric actuators to squeeze the fluid in the desired direction without check valves or specially

Supported by National Natural Science Foundation of China (Grant No. 51305439) and Jiangsu Provincial Natural Science Foundation of China (Grant No. BK20141205).

✉ Yu-Ting Ma
mayt@sibet.ac.cn

[1] CAS Key Lab of Bio-Medical Diagnostics, Suzhou Institute of Biomedical Engineering and Technology, Chinese Academy of Sciences, Suzhou 215163, China

designed ports. Traveling wave pump, introduced by Barcohen and Chang [10], utilizes multiple chambers between the crests of the traveling wave to offer a platform for the transportation of captured gas or fluid in the direction of the wave propagation.

In order to characterize and optimize the performance of piezoelectric pumps, lots of numerical and experimental studies have been performed. Kang, et al [11] presented a design guideline for a piezoelectric actuated check valve diaphragm pump. The relationship between the stroke volume and backpressure of a check valve diaphragm pump was simulated with finite element analysis tool. Goldschmidtboing, et al [12] developed a fluidic model for micro-diaphragm pumps with active valves by a lumped-parameter approach. A single equation describing the whole flow versus backpressure and frequency characteristic was deduced. A valveless piezoelectric pump with multistage Y-shape treelike bifurcate tubes was designed by Huang, et al [13]. Theoretical analysis and numerical simulation using CFX on flow resistance characteristics and the flow rate of the pump were performed. The 2D and 3D analysis on the pump with fractal-like Y-shape branching tubes were also conducted [14, 15]. Wang, et al [16], discussed on the loss characteristics and flow rectification performance of flat-walled micro-diffuser valves with change of entrance geometry and Reynolds number. Sayar and Farouk [17] developed a comprehensive numerical model for the coupled multifield analysis of piezoelectrically actuated valve-less micropump, predicting the influence of actuation frequency and applied voltage on the flow rates with the effects due to compressibility included. The flow rate spectra of the two peristaltic micropumps were modeled numerically using an electronic–hydraulic analogy by Hsu, et al [18]. The results have shown that the numerical predictions for the maximum flow rate of the two micropumps are in good agreement with the exact values. Simulation analysis and experimental verification of spiral-tube-type valveless piezoelectric pump with gyroscopic effect were presented by Leng, et al [19]. Tabak and Yesilyurt [20] presented a simulation-based analysis of transient, two-dimensional stokes flow induced by propagation of sinusoidal deformations on an elastic thin-film submerged in a fluid between parallel plates.

The piezoelectric pumps with check valves usually have problems of fatigue, clogging, and low frequency responses of check valves. Compared with passive check valves, piezoelectric active valves (such as piezoelectric stack or piezoelectric slice type active valves) [12, 21] increase the operating frequency of the pump, but coordinating the operation of pump vibrator and valve vibrator in high frequency pumping is difficult. Moreover, the valve control system is complex and difficult in integrated design. Using MEMS technology to produce new check valves [22–24] with excellent high frequency characteristics is an alternative method, but the manufacture and control of these micro valves have several drawbacks, e.g., complex design, difficult manufacturing and short life time. Conventional valveless micropumps usually use specially designed ports to rectify flow. They output fluid in one direction by difference of flow volume transported through outlet and inlet ports. Thus, these ports do not completely have a one-way flow. Energy loss and liquid reflux are serious [16, 18].

Piezoelectric centrifugal pump is a new type of piezoelectrically actuated pump that is different from previously reported pumps in principle [25]. Several piezoelectric elements attached to the metal tube are used as the actuators to push the metal tube to swing at its first bending resonant frequency. The centrifugal force generated by the swinging motion will force the liquid out of the metal tube. The pump has advantages of simple structure and convenient control. It does not need any flow valve or special inlet/outlet. Liquid flows stably, and it's particularly well suited to high-frequency pumping. With improvement of the piezoelectric elements manufacturing, both the micropump and medium-sized pumps can be generated based on this structure. The micro-pump based on this structure may be used in small parts cleaning and adhesive spraying. Micro-pumps using carbon nanotubes may also be created. Small and medium-sized pumps based on this structure can be used in decorative fountains.

This paper addresses the development of a comprehensive numerical model for the coupled multi-field analysis of the piezoelectric centrifugal pump mentioned in Ref. [25]. Flow generated from the pump was modeled using mechanical equations of motion for the solids, the electromechanical field equations for the actuator, and mass/momentum conservation equations for the fluid. The solid and fluid domains were coupled by the bending mode of metal tube, which was also the moving boundary of fluid domain. The bending resonant frequency, bending mode, and centrifugal force in solid domain were presented; the liquid flow rate, velocity profile, and gauge pressure were investigated in fluid domain. The working frequency and flow rate as functions of different component sizes were discussed and verified through experiments to guide the pump design.

2 Centrifugal Pump Model

The centrifugal pump consists of a metal tube as the flow channel and two piezoelectric sheets as the actuators. As shown in Fig. 1(a), the upper and lower piezoelectric sheets were adhered symmetrically with respect to the middle metal tube. The bottom part of the outer wall of the

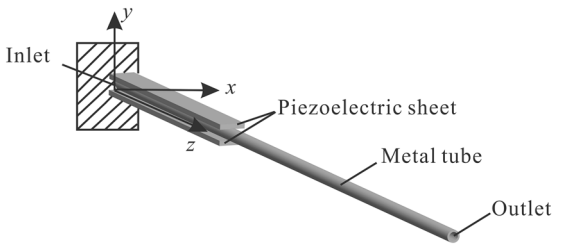

(a) Components and boundary conditions

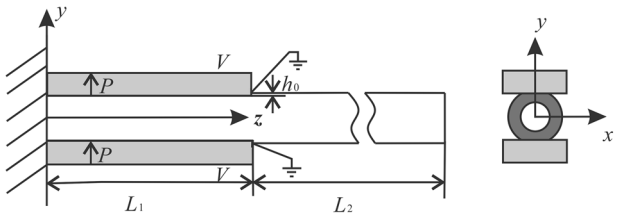

(b) Poling and driving method

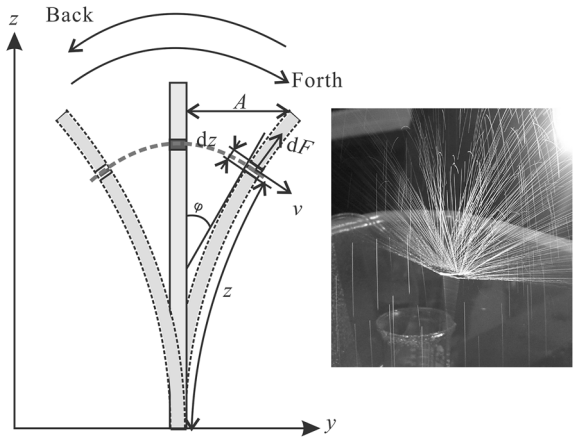

(c) Swinging back and forth motion

Fig. 1 Schematic representations of the centrifugal pump

metal tube was polished to ensure that the piezoelectric sheets and the metal tube make surface contact to benefit force transmission. Each piezoelectric sheet was fully covered by electrodes at its two surfaces perpendicular to y axis. The common end of piezoelectric sheets and metal tube was fixed, and another end was free to move.

The two piezoelectric sheets could be arranged in the same poling direction, as shown in Fig. 1(b), with the arrow and symbol P denoting the polarization direction of the piezoelectric sheets. Electrodes of piezoelectric sheets attached to the metal tube were grounded, and another two electrodes were excited with the same voltage signal. When a sinusoidal voltage was applied, piezoelectric sheets produced transverse bending vibration and drove the metal tube to swing back and forth correspondingly, as shown in Fig. 1(c). If the driving voltage is at the first bending resonant frequency of the system, the swing amplitude A of the metal tube will be greatly amplified, which means the liquid segment obtains a large tangential velocity v and the resultant centrifugal force dF is also large. As the direction of centrifugal force is always vertical to linear velocity, it is along the axis of tube all the time even if the angular velocity changes. Besides, no matter how the metal tube swings (back or forth), the directions of the obtained centrifugal forces are both towards the free end of the tube. If the total centrifugal force is large enough to overcome resistance, such as gravity and viscous damping, then the liquid in the metal tube can be forced out of the free end of metal tube, as shown in Fig. 1(c). The metal tube should be filled with liquid for initialization. A check valve can be added to prevent liquid from flowing backward in gravity when the pump stops running, thereby avoiding repeated initialization of the pump. The check valve has no influence on the working frequency of the pump because the valve is always open during pumping.

3 Mathematical Model

Piezoelectrically actuated pump design and analysis is a complex multidisciplinary problem with field couplings in electrical, mechanical, and fluid quantities. The governing equations for the solid and fluid domains, as well as the boundary and initial conditions, are discussed. In addition, the coupling relations of the mechanical, electrical, and fluid fields are described in the following sections.

3.1 Solid Domain

In this domain, the piezoelectric sheet, metal tube and working liquid are all considered in aspect of their influences on dynamic vibration of the pump. It is supposed that the thickness of the structure remains constant after deformation, and the axial displacement is caused by the bending angle and the height in thickness coordinate. The piezoelectric sheet and steel tube make good surface contact and there is no slippage between them. Subscript of vector 1, 2, 3 in the following equations denotes their components in z, x, y directions, respectively. Equations of bending displacement and angle can be formulated as [26]

$$\begin{cases} u_1 = \varphi y, \\ u_2 = 0, \\ u_3 = -\varpi(z), \\ \varphi = \mathrm{d}\varpi/\mathrm{d}z, \end{cases} \tag{1}$$

where u_1, u_2, u_3 denote displacements in z, x, and y directions; φ represents the bending angle; ϖ is the displacement function need to be solved, which changes with

z. For a segment with length of dz, z is its distance away from fixed end; φ is the angle between the tangential line and vertical line, as shown in Fig. 1(c). Piezoelectric constitutive equations revealing electromechanical coupling are given by

$$\begin{cases} S_1 = s_{11}^{\mathrm{E}} T_1 + d_{31} E_3, \\ D_3 = d_{31} T_1 + \varepsilon_{33}^{\mathrm{T}} E_3, \end{cases} \tag{2}$$

where s_{11}^{E} is the elastic compliance constant; T_1 and S_1 are stress and strain in z axis; d_{31} is the piezoelectric constant; E_3 is the electric field intensity; $\varepsilon_{33}^{\mathrm{T}}$ is the dielectric permittivity constant; D_3 is the electric displacement in y axis. Superscripts E and T denote the quantity at constant electric field and at constant stress, respectively. For metal material

$$S_1 = T_1 / Y_{\mathrm{m}}, \tag{3}$$

where Y_{m} is Young's modulus of elastic material. Quasi-static electric condition is

$$\mathrm{d}D_3/\mathrm{d}y = 0. \tag{4}$$

Relationship between electrical field and electrical potential ψ is

$$E_3 = -\mathrm{d}\psi/\mathrm{d}y. \tag{5}$$

The electric potential, stress, electric field intensity, and electric displacement are functions of y coordinate and can be expressed as

$$\begin{cases} \psi = \psi^{(0)} + y\psi^{(1)} + y^2\psi^{(2)}, \\ E_3 = E_3^{(0)} + yE_3^{(1)}, \\ T_1 = T_1^{(0)} + yT_1^{(1)}, \\ D_3 = D_3^{(0)} + yD_3^{(1)}, \end{cases} \tag{6}$$

where superscripts (0), (1), and (2) denote the order of the expansion terms in relation to thickness coordinate y. Considering the boundary condition:

$$\begin{cases} \psi = V, & y = (R_{\mathrm{o}} - h_0 + h), -(R_o - h_0 + h), \\ \psi = 0, & y = (R_{\mathrm{o}} - h_0), -(R_o - h_0), \end{cases} \tag{7}$$

where h is the thickness of piezoelectric sheet; h_0 is the removed thickness of outer wall of the metal tube; R_{o} is the outer radius of metal tube; V is the driving voltage applied to the electrode.

The stress and electrical displacement can be solved as functions of displacement and applied voltage by substituting Eqs. (1), (4)−(7) into Eqs. (2) and (3). For the part with length L_1, T_1 and D_3 can be represented as: For piezoelectric material, when $R_{\mathrm{o}} - h_0 < y < R_{\mathrm{o}} + h - h_0$,

$$\begin{cases} T_1^{(0)} = -\dfrac{k_{31}^2(2R_{\mathrm{o}} + h - 2h_0)\gamma}{2s_{11}^{\mathrm{E}}(1-k_{31}^2)} + \dfrac{d_{31}V}{s_{11}^{\mathrm{E}}h}, \\ T_1^{(1)} = \dfrac{\gamma}{s_{11}^{\mathrm{E}}(1-k_{31}^2)}, \\ D_3^{(0)} = \dfrac{(2R_{\mathrm{o}} + h - 2h_0)d_{31}\gamma}{2s_{11}^{\mathrm{E}}} - \dfrac{\varepsilon_{33}^{\mathrm{T}}(1-k_{31}^2)V}{h}, \\ D_3^{(1)} = 0. \end{cases} \tag{8}$$

For metal material, when $0 < y < R_{\mathrm{o}} - h_0$,

$$\begin{cases} T_1^{(0)} = 0, \\ T_1^{(1)} = Y_{\mathrm{m}}\gamma, \\ D_3 = 0, \end{cases} \tag{9}$$

where $k_{31}^2 = d_{31}^2/s_{11}^{\mathrm{E}}\varepsilon_{33}^{\mathrm{T}}$, $\gamma = \mathrm{d}^2\varpi/\mathrm{d}z^2$. For the part with length L_2 with only metal material, when $0 < y < R_{\mathrm{o}}$, T_1 and D_3 can be represented as

$$\begin{cases} T_1^{(0)} = 0, \\ T_1^{(1)} = Y_{\mathrm{m}}\gamma, \\ D_3 = 0. \end{cases} \tag{10}$$

The equation of equilibrium is

$$\mathrm{d}^2M/\mathrm{d}z^2 = \rho A\omega^2\varpi, \tag{11}$$

where M is the bending moment. For the part with length of L_1,

$$M = m\gamma + nV, \tag{12}$$

where $\rho A = \rho_{\mathrm{p}}S_{\mathrm{p}} + \rho_{\mathrm{m}}S_{\mathrm{m}} + \rho_{\mathrm{l}}S_{\mathrm{l}}$,

$$m = \frac{4\left[(R_o - h_0 + h)^3 - (R_o - h_0)^3\right]}{6s_{11}^{\mathrm{E}}(1-k_{31}^2)} - \frac{3k_{31}^2 h[h + 2(R_o - h_0)]^2}{6s_{11}^{\mathrm{E}}(1-k_{31}^2)} + \frac{Y_m(R_o - h_0)R_o^3}{8}\cos 2\theta \sin\theta + \frac{R_o^4}{8}\left(\frac{\pi}{2} - \theta\right),$$

$$n = d_{31}(2R_o + h - 2h_0)w/s_{11}^{\mathrm{E}},$$

w is the width of piezoelectric sheet; R_{i} is the inner radius of metal tube; ρ_{p}, ρ_{m} and ρ_{l} are the densities of piezoelectric sheet, metal tube, and working liquid, respectively; S_{p}, S_{m} and S_{l} are the cross section area of the piezoelectric sheet, metal tube, and working liquid, respectively. $\theta = \arccos((R_{\mathrm{o}} - h_0)/R_{\mathrm{o}})$. For the part with length of L_2,

$$M = m\gamma, \tag{13}$$

where $m = Y_{\mathrm{m}}\pi(R_{\mathrm{o}}^4 - R_{\mathrm{i}}^4)/4$, $\rho A = \rho_{\mathrm{m}}S_{\mathrm{m}} + \rho_{\mathrm{l}}S_{\mathrm{l}}$.

Substituting Eqs. (12)−(13) into Eq. (11), a fourth order differential equation can be obtained:

$$\mathrm{d}^4\varpi/\mathrm{d}z^4 = \beta^4\varpi, \tag{14}$$

where

$$\beta = \left(\rho A\omega^2/m\right)^{1/4},$$

ω is the angular frequency.

The boundary condition is

$$\begin{cases} \varpi_1(0) = 0, \\ \varpi_1'(0) = 0, \\ M_2(L_2) = 0, \\ Q_2(L_2) = 0, \end{cases} \tag{15}$$

where Q is the shear force. The continuity condition for the two parts with length of L_1 and L_2 is

$$\begin{cases} \varpi_1(L_1) = \varpi_2(L_1), \\ \varpi_1'(L_1) = \varpi_2'(L_1), \\ M_1(L_1) = M_2(L_1), \\ Q_1(L_1) = Q_2(L_1). \end{cases} \tag{16}$$

Equation (14) can be solved by meeting the conditions of Eqs. (15) and (16) [24]. Thus the bending resonant frequency and bending mode shape can be obtained. Meanwhile, the centrifugal force can be calculated by

$$\begin{aligned} F = &\int_0^{L_1} \frac{\rho_l \pi R_i^2}{z} \varpi_1^2(z)\omega^2 \cos^2(\omega t)\mathrm{d}z \\ &+ \int_{L_1}^{L_1+L_2} \frac{\rho_l \pi R_i^2}{z} \varpi_2^2(z)\omega^2 \cos^2(\omega t)\mathrm{d}z. \end{aligned} \tag{17}$$

Based on the above deduction, theoretical results of the first bending resonant frequency and bending mode can be obtained by MATLAB programming.

3.2 Fluid Domain

In fluid domain, the flowing liquid has a very low Reynolds number. It is supposed that no flow occurs in the direction perpendicular to the vibrating plane (x-axis direction) [17, 20, 27], so a simplified two-dimensional model is established, as shown in Fig. 2. This two-dimensional model is composed of static part that represents liquid channel, swinging part that represents metal tube, and working space. Two phases of fluid, namely, the working liquid and gas environment, are included. Water is adopted as the working liquid, which is assumed to be viscous, incompressible Newton fluid. Air is used as gas substance, which is viscous, compressible Newton fluid. The governing equations, which include the Navier-Stokes equations of balance of linear momentum and the continuity equation, can be written as

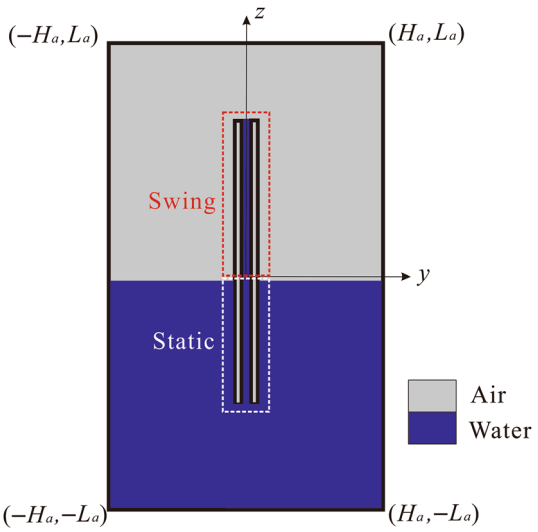

Fig. 2 Two-dimensional fluid domain of centrifugal pump

$$\frac{\partial(\rho\mathbf{u})}{\partial t} + \nabla\cdot(\rho\mathbf{u}\mathbf{u}) = -\nabla P + \mu\nabla^2\mathbf{u}, \tag{18}$$

$$\frac{\partial\rho}{\partial t} + \nabla\cdot(\rho\mathbf{u}) = 0, \tag{19}$$

where $\boldsymbol{u} = [v, w]'$ is the velocity vector, ρ is fluid density, P is pressure, and μ is molecular viscosity. The time-dependent domain is the volume occupied by fluid at time t, and defined by boundaries of static wall, pressure outlet, and moving wall that coincides with oscillation of metal tube.

The left, right, and bottom boundary of fluid domain and the liquid channel are static walls. No-slip conditions on the static walls are as follows

$$\begin{cases} v(H_\mathrm{a}, z, t) = w(H_\mathrm{a}, z, t) = 0, \\ v(-H_\mathrm{a}, z, t) = w(-H_\mathrm{a}, z, t) = 0, \\ v(y, -L_\mathrm{a}, t) = w(y, -L_\mathrm{a}, t) = 0, \\ v_\mathrm{static}(y, z, t) = w_\mathrm{static}(y, z, t) = 0, \end{cases} \tag{20}$$

where v_static and w_static refer to the velocity of static part of liquid channel, as shown in Fig. 2.

Fluid velocity on moving boundaries of vibrating tube is equal to the time-derivative of corresponding displacement for the y and z direction components:

$$\begin{cases} v_\mathrm{swing}(y, z, t) = -\dfrac{\mathrm{d}\varpi}{\mathrm{d}t}, \\ w_\mathrm{swing}(y, z, t) = y\cdot\dfrac{\mathrm{d}^2\varpi}{\mathrm{d}z\cdot\mathrm{d}t}, \end{cases} \tag{21}$$

where v_swing and w_swing refer to the velocity of swing part of liquid channel, as shown in Fig. 2. They can be calculated by the bending mode ϖ got in Sect. 3.1.

Outlet pressure of upper boundary of fluid domain is set to zero

$$[-P\mathbf{I}] \cdot \mathbf{n}\big|_{y,L_a,t} = 0, \tag{22}$$

where $\boldsymbol{n}$ is the outward normal of the surface. The initial condition for Eq. (19) is for all the velocity components to be zero at $t = 0$

$$v(y, z, 0) = w(y, z, 0) = 0. \tag{23}$$

In the numerical calculation process of fluid domain, the motion of the metal tube is transmitted to the fluid region through Eq. (21) at the fluid solid interface, which yields the altered flow domains in every iterative calculation. The fluid velocities and pressures are computed using Eqs. (18) and (19) with boundaries of Eqs. (20)−(22) and initial conditions of Eq. (23).

As the static channel is relatively steady and axisymmetric to its central axis, the instantaneous flow rate of the pump can be calculated by rotating the two-dimensional velocity curve $\boldsymbol{u}(t)$ in the static channel with respect to z-axis to construct the three-dimensional surface velocity $\boldsymbol{U}(t)$. Then the instantaneous flow rate can be computed by surface integrating of fluid velocity $\boldsymbol{U}(t)$ in z axis over liquid channel cross section

$$Q_{\{\text{in,out}\}}(t) = \iint_S \mathbf{U}(t) \cdot (-\mathbf{n}_{\text{in}}) \mathrm{d}s, \tag{24}$$

where $\boldsymbol{n}_{\text{in}}$ corresponds to inlet surface normal, and "–" signs defines inlet flows. Time-averaged flow rate can be computed by integrating the instantaneous flow rate over a suitable time interval. It is preferred that the calculation is made after the initial ramp is completed and the period should be long enough to capture at least one entire cycle

$$Q_{\text{av}\{\text{in,out}\}} = \frac{1}{t_1 - t_0} \int_{t_0}^{t_1} Q_{\{\text{in,out}\}}(t) \mathrm{d}t. \tag{25}$$

A two-dimensional model was built for analysis in software FLUENT. In our previous work, the flow rate in a tube with inner diameter of 0.7 mm is 7.7 mL/min, so the Reynolds number is calculated to be 234, which is much smaller than 2300. The effect of the air motion, which has about 1000 times smaller inertia, can be negligible as well. Therefore, volume of fluid model (VOF model) with implicit scheme and laminar model were used. The governing equations for the liquid domain were solved using the SIMPLE algorithm. Terms for the discretization of convection terms were formulated according to the second-order accurate upwind scheme for momentum. For the flows with deforming boundaries, grid was updated at every time step. Dynamic meshing was introduced by spring smoothing and re-meshing method based on arbitrary Lagrangian–Eulerian scheme, which determined the node distribution based on the motion of the boundary nodes. Triangle unstructured elements were used for dynamic re-meshing. For the basic model, the total element number was 135196 with domain size of 600 mm × 450 mm. The problem was simulated using 60 time steps per cycle. Increasing the element number or time step did not have any appreciable effect on the results. The simulated results were stored for each step. If the dimensionless residuals in all grid points were less than 10^{-5}, the calculation was assumed to be converged. Total computation time per case was approximately 10 h on a Lenovo computer equipped with Intel Core i3 processor and 4.0 GB of memory.

3.3 Material and Working Fluid Properties

Material properties and working fluid properties considered are listed in Table 1. Property data are given below for the piezoelectric material (PZT-4), metal tube (stainless steel), and working fluid (water and air).

4 Experiment Prototypes

Pump prototypes were fabricated to validate theoretic and simulated results. The basic prototype was 80, 1.0, and 0.15 mm for the length, outer diameter, and thickness of metal tube, respectively; whereas 30, 5, and 0.4 mm were for the length, width, and thickness of piezoelectric sheet. The bottom part of the outer wall of the metal tube was

Table 1 Material and fluid properties for centrifugal pump analysis

Material	Parameter	Value
Stainless steel	Density ρ_m/(kg·m^{-3})	7850
	Young's modulus Y_m/GPa	210
	Poisson's ratio ν_m	0.30
Water	Density ρ_l/(kg·m^{-3})	998.2
	Kinematic viscosity γ_l/(kg·(m·s)$^{-1}$)	0.001
Air	Density ρ_a/(kg·m^{-3})	1.225
	Kinematic viscosity γ_a/(kg·(m·s)$^{-1}$)	1.79×10^{-5}
PZT-4	Density ρ_p/(kg·m^{-3})	7500
	Relative permittivity ε_{11}^S	730
	Relative permittivity ε_{33}^S	635
	Piezoelectric constant e_{31}/(C·m^{-2})	-5.2
	Piezoelectric constant e_{33}/(C·m^{-2})	15.1
	Piezoelectric constant e_{15}/(C·m^{-2})	12.7
	Stiffness c_{11}^E/(GN·m^{-2})	139
	Stiffness c_{12}^E/(GN·m^{-2})	77.8
	Stiffness c_{13}^E/(GN·m^{-2})	74.3
	Stiffness c_{33}^E/(GN·m^{-2})	115
	Stiffness c_{44}^E/(GN·m^{-2})	25.6
	Stiffness c_{66}^E/(GN·m^{-2})	30.6

polished to ensure that the piezoelectric sheets and the metal tube make surface contact to benefit force transmission. The piezoelectric sheets made of PZT-4 were supplied by the Hunan Jiayeda Electronics Company and were cut to desired shape by automatic dicing saw (DISCO DAD 3350). Two PZT sheets were attached symmetrically to the outer surface of steel tube with epoxy adhesive (3 M DP460), ensuring that PZT sheets were arranged parallel to the axial direction of steel tube. The common ends of PZT sheets and steel tube were fastened to a steel basement with epoxy adhesive. A rubber pipe linked to the fixed end of the steel tube was used as liquid channel. A check valve was added in the liquid channel to facilitate initialization. Figure 3 shows a photograph of the basic pump prototype. In addition, many prototypes with different component sizes were fabricated and tested for comparison. In experiments, the rubber pipe was connected to a water tank. The mass reduction of the water tank measured by an electronic balance (resolution: 0.1 g) was divided by the time interval to obtain the average flow rate.

5 Results and Discussion

5.1 Dynamics of Vibration

The first bending resonant frequencies as functions of dimensional parameters are plotted in Figs. 4(a)–(e).The investigated dimensional parameters are the length and outer diameter of metal tube, as well as the length, width, and thickness of piezoelectric sheet. The basic model is 80 mm and 1.0 mm for the length and outer diameter of metal tube, respectively, whereas 30, 5, and 0.4 mm are for the length, width, and thickness of piezoelectric sheet, respectively, which corresponds to the basic prototype. In Fig. 4, only one dimensional parameter changes while others are kept constant. The outer diameter and inner diameters of the metal tube are changed synchronously without changing wall thickness of 0.15 mm.

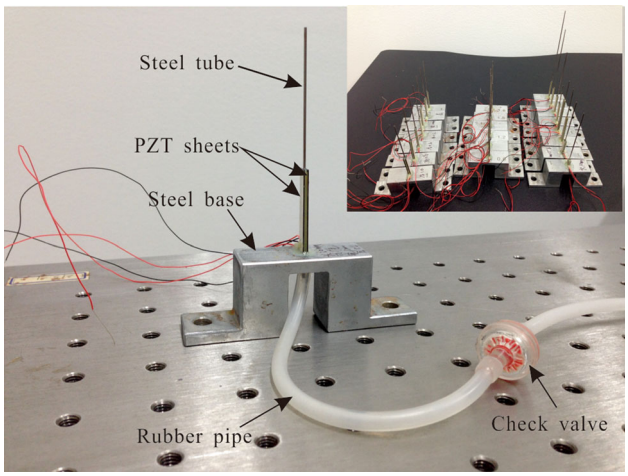

Fig. 3 Experimental pump prototypes

From Figs. 4(a) and (b), the resonant frequency of the pump increases when piezoelectric sheet width or thickness becomes larger. Placed at the fixed end of pump, PZT sheets increase the system stiffness. Thus, rigidity improvement is enhanced with increase of thickness or width of the ceramic sheet, which leads to increase of resonant frequency. Figure 4(c) shows that an optimal value of piezoelectric sheet length is available to obtain the maximum resonant frequency. It is because PZT sheets close to the fixed end increase system stiffness, whereas PZT sheets close to the free end increase system mass. These two factors have reverse effects on the bending resonant frequency. Thus, the second factor gradually replaces the dominant role of the first factor as the PZT sheet length increases, which results in an optimal value of PZT sheet length for the largest resonant frequency. Figures. 4(d) and (e) shows that the resonant frequency of pump declines with increase of metal tube length, and it rises with increase of metal tube diameter. This changing trend is similar to that of a single tube. System mass increases and stiffness decreases for the case in Fig. 4(d). Both system mass and stiffness increase for the case in Fig. 4(e), but the effect of stiffness improvement overtakes that of mass. In general, theoretical calculated resonant frequencies agree well with experimental results.

Bending mode of the basic model according to theoretical deduction is shown in Fig. 5, with normalized transverse displacement compared with that of single metal tube filled with water. It can be seen that section L1 with PZT sheets attached has a larger rigidity, thus, its vibrating amplitude is much smaller than that of section L2. Transverse displacement increases abruptly at the free end of the piezoelectric sheets, and the resulting strain is the largest. It can be predicted that the largest stress intensity is also located here.

5.2 Flow Rate

In Fig. 6, time-dependent axial (in z-axis direction) flow velocity at liquid channel center of the basic model is shown with resonant frequency of 298.4 Hz, driving voltage amplitude of 80 V_{pp} and backpressure of 0.8 kPa. The static liquid channel is 0.05 m and the axial flow velocity is probed at 0.02 m from its inlet port. When the pump starts vibrating, flow velocity climbs quickly, and the growth rate gradually slows down until a steady-periodic state is reached after approximately 25 cycles. The steady-periodic state solutions are confirmed by the negligible standard deviation between velocity profiles for the same phases during several consecutive cycles. With the increase of

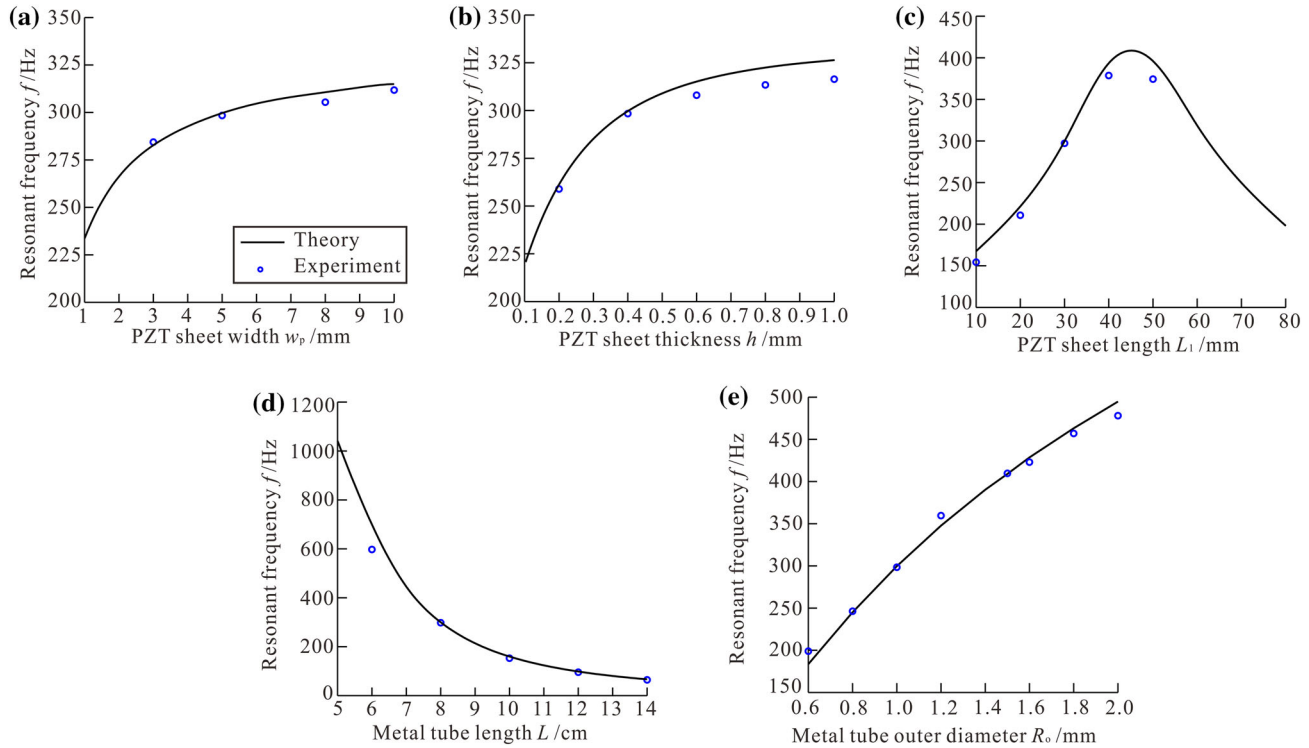

Fig. 4 First bending resonant frequency of the pump filled with water for (a) varying PZT sheet width, (b) PZT sheet thickness, (c) PZT sheet length, (d) metal tube length and (e) metal tube diameter

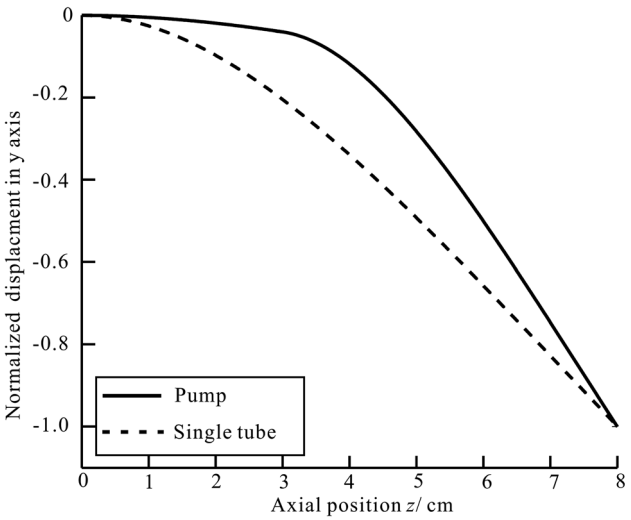

Fig. 5 Bending mode of the basic model of pump compared with a single tube

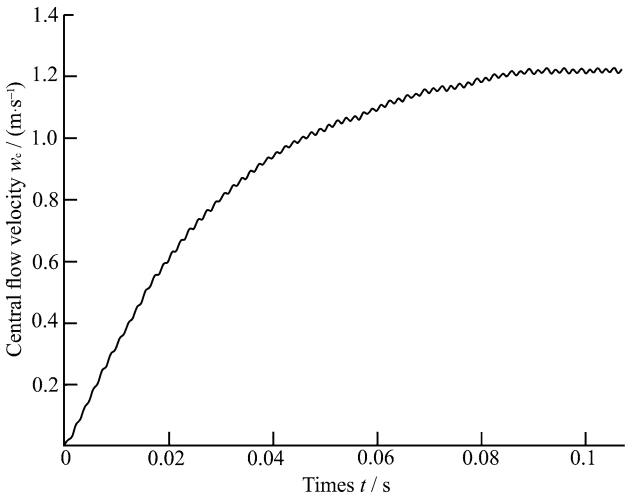

Fig. 6 Time-dependent axial flow velocity at liquid channel center, $f = 298.4$ Hz and $V_{pp} = 80$ V, lasting for $t = 0.1006$ s including 30 cycles

liquid velocity, viscous damping in the metal tube also increases until gravity and viscous damping balance the driving force, and the flow velocity achieves maximum, remaining relatively steady afterward.

In Fig. 7, time-dependent axial flow velocity at liquid channel center (0.02 m from inlet port of static liquid channel) of the basic model is shown in the 30th cycle. It can be regarded as cyclical swinging velocity added to a bias velocity. The bias velocity of 1.213 m/s is the accumulation of previous 29 cycles. The swinging velocity profile is mainly composed of two sinusoidal waveforms, with one lasting for a longer period of time and presenting a larger amplitude than the other. This is reasonable because one vibrating cycle is not an integer multiples of time step, which results in different number of time steps calculated for two sides of oscillation. When the metal tube

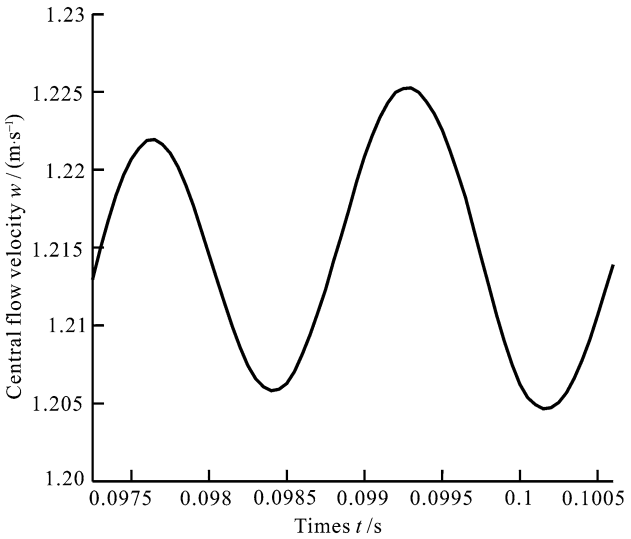

Fig. 7 Time-dependent axial flow velocity at liquid channel center in the 30th cycle, $f = 298.4$ Hz and $V_{pp} = 80$ V

arrives at the position of maximum amplitude (limit position), the vibrating velocity is zero, so the axial flow acceleration reaches the maximum negative value. When the metal tube arrives at the position of zero amplitude (original position), the vibrating velocity is maximum, so the axial flow acceleration reaches the maximum positive value. When the metal tube moves from the original position to limit position, axial flow acceleration gradually decreases, so a positive flow velocity peak appears. A negative flow velocity peak appears for the same reason when the metal tube moves in reverse direction.

Figure 8 shows the axial flow velocity profile as functions of distance from the tube axis (z-axis) and applied voltages in the static liquid channel, at the end of 30th cycle, $t = 0.1006$ s. The investigated polyline is probed at 0.02 m from inlet port. Actuation frequency is kept constant at 298.4 Hz, and peak to peak actuation voltages vary between 80.0 V and 144 V. A parabolic velocity profile is observed in Fig. 8. The generated flow increases as the driving electrical potential of PZT sheets increases.

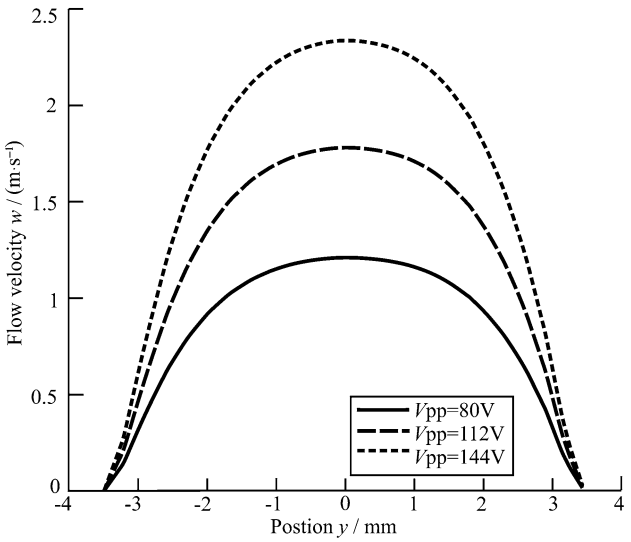

Fig. 8 Axial flow velocity of the basic model along liquid channel cross section at the end of the 30th cycle, $t = 0.1006$ s, $V_{pp} = 80$ V, 112 V and 144 V

Figure 9 shows varying contours of gauge pressure field for the basic model during the 30th cycle. The flow channel is compressed to one-tenth of the original length to facilitate observation, although a little distortion is found in Tecplot 360. When the vibrating tube arrives at the original position, the largest negative pressure in the tube causes the largest flow acceleration. When the tube moves to the limit position, negative pressure in the tube is reduced, and a positive pressure field is generated on one side of the tube; thus, a decreasing flow acceleration along positive z axis is produced, and a flow acceleration along y axis is generated against the movement of tube. Therefore, the flow velocity in y axis is gradually reduced. When the tube moves from the limit position to the original position, an increasing flow acceleration along positive z axis is produced, and a flow acceleration along y axis is produced following the movement of tube; thus, the flow velocity in y axis is increased. The above conclusion is in accordance with the results shown in Fig. 7. The pressure in the static liquid channel is always symmetric to z axis; thus, the velocity distribution in static liquid channel is also symmetric. However, the velocity profile in the vibrating tube shows asymmetric shape according to the movement direction.

If the multiple of vibrating amplitude A and frequency f of the metal tube is defined as power coefficient, then the time-averaged flow rate and power coefficients of pumps as functions of dimensional parameters are plotted in

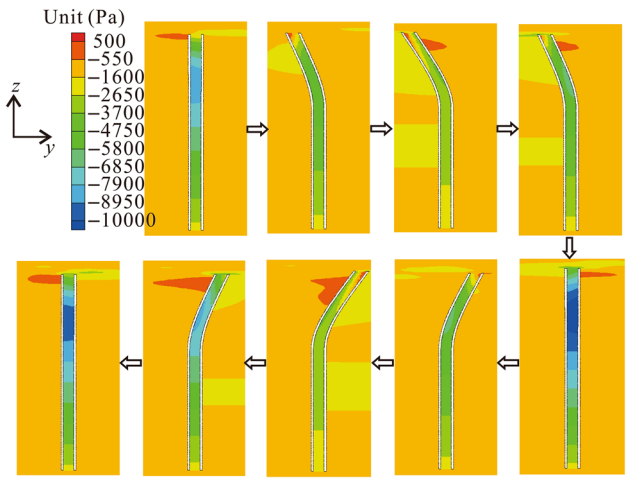

Fig. 9 Contours of gauge pressure variation for the basic model in one-eighth cycle step during the 30th cycle, $f = 298.4$ Hz and $V_{pp} = 80$ V

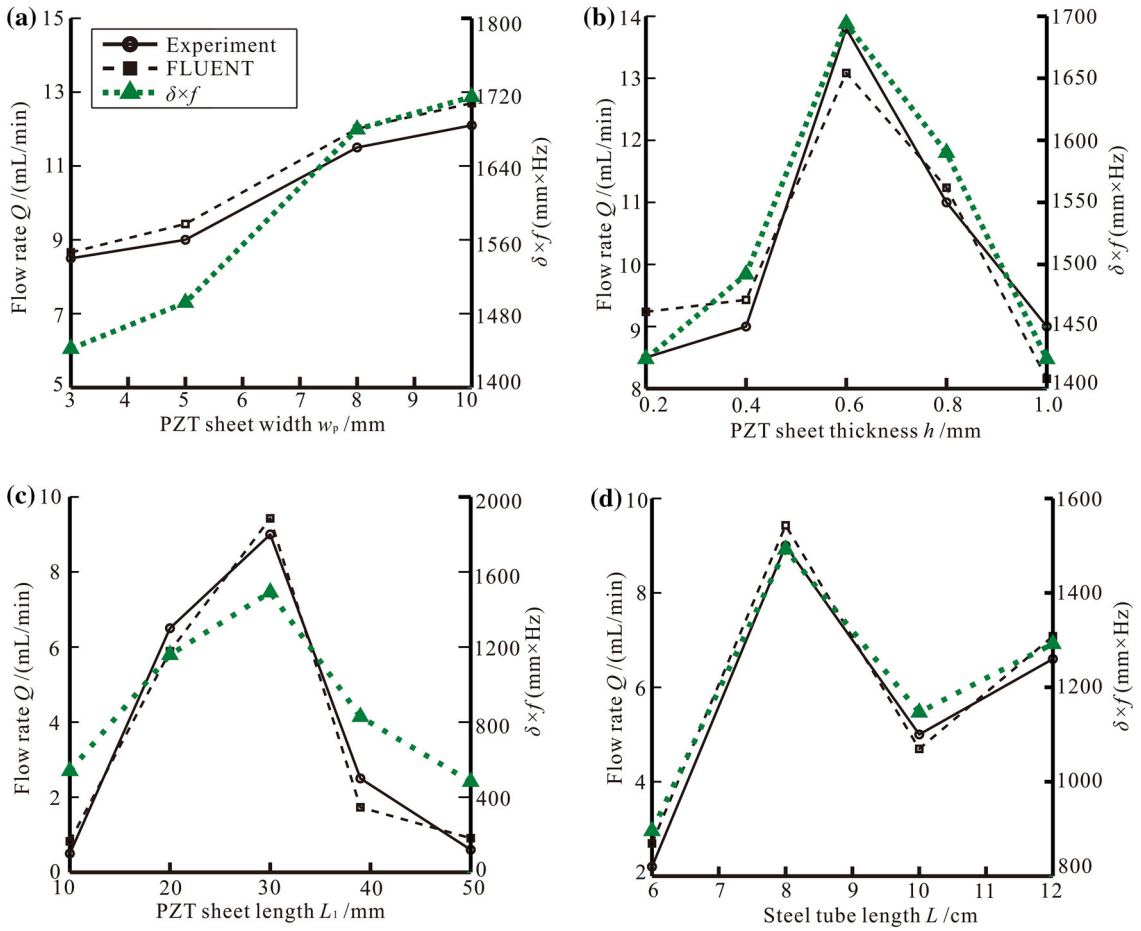

Fig. 10 Time-averaged flow rate and power coefficients of pumps for (a) varying PZT sheet width, (b) PZT sheet thickness, (c) PZT sheet length and (d) metal tube length

Figs. 10(a)−(d). The investigated dimensional parameters are the length of metal tube, as well as the length, width, and thickness of piezoelectric sheet. In Fig. 10, only one dimensional parameter changes whereas the others are kept constant. All simulations and experiments were conducted with a backpressure of 0.8 kPa.

When the vibrating tube moves away from the original position, we can anticipate that every point in the flow channel presents a similar time dependent velocity profile shown in Fig. 7. The positive and negative velocity changes relative to the velocity in the original position are theoretically equal, and their contribution to average flow rate can be canceled. Thus, average flow rates in simulation are calculated by surface integral of the parabolic velocity profile at the original position over pump cross section according to Eqs. (24)−(25). Figure 10(a) shows that the pumping flow rate increases with growth of piezoelectric sheet width. The reason is both vibrating frequency and amplitude of the metal tube increase when piezoelectric sheet width becomes larger. Figure 10(b) shows that an optimal piezoelectric sheet thickness is available to obtain the largest flow rate under the same driving electric field intensity of 200 V/mm. When piezoelectric sheet thickness increases, vibrating frequency increases and vibrating amplitude decreases, so an optimal value exists to generate the maximum driving force. The prototype with PZT sheet thickness of 0.6 mm presents the largest flow rate of 13.8 mL/min. Figures 10(c) and (d) illustrate that the length of piezoelectric sheet and metal tube should match to generate the largest flow rate. It is already known from Fig. 4(c) that, as the length of PZT sheet becomes larger, the resonant frequency first increases and then decreases. The vibrating amplitude decreases as the PZT sheet length increases. From Fig. 4(c), the largest flow rate can be expected to occur when the PZT sheet length is smaller than 45 mm. Simulated and experiment results show that the prototype with PZT sheet length of 30 mm exhibits the largest flow rate of 9 mL/min. When the length of metal tube becomes larger, the resonant frequency decreases and the vibrating amplitude becomes larger. Thus, an optimal value exists to generate the maximum driving force. Figures 10(a)−(c) shows that, the change of power

coefficients is similar to that of the flow rate. According to Eq. (17), if the vibration modes of different tested prototypes are similar, then the centrifugal force is proportional to the square of vibrating amplitude and frequency multiples. Our previous study reached the same conclusion [25]. Therefore, a prototype with a large power coefficient can produce a large flow rate when the influence of viscous damping and gravity is not significant. In Fig. 10(d), flow rate is not only influenced by power coefficient but also related to resistance. As the tube length grows, gravity and viscous damping both become larger. So the prototype with tube length of 120 mm, which has a higher power coefficient, presents a smaller flow rate than that of the prototype with tube length of 100 mm. We also tested the prototype pumps with different metal tube outer diameters of 0.6, 0.8, 1.0, 1.2, and 1.5 mm with the same thickness of 0.15 mm. The prototypes with outer diameters of 0.6 mm and 0.8 mm present flow rate of 2.4 mL/min and 3.5 mL/min, with power coefficient of 1890.5 and 1354.7, respectively. The prototype with tube outer diameters of 0.6 mm has larger power coefficient, but outputs smaller flow. It is because the viscous damping in thinner tube is much larger and its effect overtakes that of driving force. Unfortunately, the prototypes with tube outer diameters larger than 1 mm have no output, because gravity of liquid in these tubes are large and power coefficient is relatively small.

In Fig. 10, simulated flow rates generally agree well with experimental results, but discrepancy is still found, which could be attributed to three reasons. First, a rubber pipe with length of 0.3 m and inner diameter of 3 mm connected the inlet of pump and water tank in experiments. Damping effect of this long pipe is not considered in simulation. However, the rubber pipe has a much larger inner diameter than pump, and the viscous damping of the rubber pipe is much smaller. Second, the pump prototypes are all made by hand and will be prone to fabricating errors concerning parallel and symmetric positioning. Third, the flow rate is measured as the average of outlet mass at a constant time period. When the flow rate is very small, evaporation of water over long time and balance error will both cause measured discrepancy.

6 Conclusions

(1) Bending mode analysis shows that the section with PZT sheets attached has a much smaller vibrating amplitude. The maximum stress is located near the free end of PZT sheet where transverse displacement increases abruptly.

(2) The exciting voltage amplitude is a dominant factor on the flow rate of pump. Pumping flow rate increases with growth of piezoelectric sheet width. An optimal piezoelectric sheet thickness is available to generate the largest flow rate under the same driving electric field intensity. The length of piezoelectric sheet and metal tube should match to generate the largest flow rate. The multiple of vibrating amplitude and frequency determines flow rate when centrifugal force is the dominant factor. Viscous damping and gravity are reasons for flow rate reduction.

(3) By solving the electro-mechanical-fluidic coupling problem, the model developed in this study can provide theoretical guidance on the optimization of centrifugal valveless pump characters.

References

1. A K Au, H Y Lai, B R Utela, et al. Microvalves and micropumps for BioMEMS. *Micromachines*, 2011, 2(2): 179–220.
2. B Iverson, S V Dgarimella. Recent advances in microscale pumping technologies: a review and evaluation. *Microfluidics and Nanofluidics*, 2008, 5(2): 145–174.
3. H K Ma, W F Luo, J Y Lin. Development of a piezoelectric micropump with novel separable design for medical applications. *Sensors and Actuators A: Physical*, 2015, 236: 57–66.
4. Z H Zhang, J W Kan, G M Cheng, et al. A piezoelectric micropump with an integrated sensor based on space-division multiplexing. *Sensors and Actuators a-Physical*, 2013, 203: 29–36.
5. Y Wei, R Torah, K Yang, et al. A novel fabrication process to realize a valveless micropump on a flexible substrate. *Smart Materials and Structures*, 2014, 23(2): 025034.
6. Z Zhang, J Kan, S Wang, et al. Effects of driving mode on the performance of multiple-chamber piezoelectric pumps with multiple actuators. *Chinese Journal of Mechanical Engineering*, 2015, 28(5): 954–963.
7. H T G Vanlintel, F C M Vandepol, S Bouwstra. A piezoelectric micropump based on micromachining of silicon. *Sensors and Actuators*, 1988, 15(2): 153–167.
8. E Stemme, G A Stemme, Valveless diffuser/nozzle-based fluid pump. *Sensors and Actuators a-Physical*, 1993, 39(2): 159–167.
9. J G Smith. Piezoelectric micropump with 3 valves working peristaltically. *Sensors and Actuators a-Physical*, 1990, 21(1–3): 203–206.
10. Y Bar-cohen, Z S Chang. Piezoelectrically actuated miniature peristaltic pump. *Proceedings of SPIE Smart Structures and Materials 2001: Smart Structures and Integrated Systems*, Newport Beach, CA, USA, March 4, 2001: 425–432.
11. J Kang, G W Kauner. Simulation and verification of a piezoelectrically actuated diaphragm for check valve micropump design. *Sensors and Actuators a-Physical*, 2011, 167(2): 512–516.
12. F Goldschmidtboing, A Doll, M Heinrichs, et al. A generic analytical model for micro-diaphragm pumps with active valves. *Journal of Micromechanics and Microengineering*, 2005, 15(4): 673–683.
13. J Huang, J Zhang, X Xun, et al. Theory and experimental verification on valveless piezoelectric pump with multistage Y-shape treelike bifurcate tubes. *Chinese Journal of Mechanical Engineering*, 2013, 26(3): 462–468.

14. J Huang, J Zhang, S Wang, et al. Analysis of the flow rate characteristics of valveless piezoelectric pump with fractal-like Y-shape branching tubes. *Chinese Journal of Mechanical Engineering*, 2014, 27(3): 628–634.
15. J Huang, J Zhang, W Shi, et al. 3D FEM analyses on flow field characteristics of the valveless piezoelectric pump. *Chinese Journal of Mechanical Engineering*, 2016, 29(4):1-7.
16. Y Wang, J Hsu, P Kuo, et al. Loss characteristics and flow rectification property of diffuser valves for micropump applications. *International Journal of Heat and Mass Transfer*, 2009, 52(1–2): 328–336.
17. E Sayar, B Farouk. Multifield analysis of a piezoelectric valveless micropump: effects of actuation frequency and electric potential. *Smart Materials and Structures*, 2012, 21(7): 075002.
18. Y Hsu, J Li, N Le. An experimental and numerical investigation into the effects of diffuser valves in polymethylmethacrylate (PMMA) peristaltic micropumps. *Sensors and Actuators a-Physical*, 2008, 148(1): 149–157.
19. X Leng, J Zhang, Y Jiang, et al. Simulation analysis and experimental verification of spiral-tube-type valveless piezoelectric pump with gyroscopic effect. *Chinese Journal of Mechanical Engineering*, 2014, 27(4): 822–829.
20. A F Tabak, S Yesilyurt. Simulation-based analysis of flow due to traveling-plane-wave deformations on elastic thin-film actuators in micropumps. *Microfluidics and Nanofluidics*, 2008, 4(6): 489–500.
21. D G Lee, S Or, G P Wcarman. Design of a piezoelectric-hydraulic pump with active valves. *Journal of Intelligent Material Systems and Structures*, 2004, 15(2): 107–115.
22. G J Liu, C L Shen, Z G Yang, et al. A disposable piezoelectric micropump with high performance for closed-loop insulin therapy system. *Sensors and Actuators a-Physical*, 2010, 163(1): 291–296.
23. A M Cardenas-valencia, J Dlutowski, J Bumgarner, et al. Development of various designs of low-power, MEMS valves for fluidic applications. *Sensors and Actuators A: Physical*, 2007, 136(1): 374–384.
24. M Seong, K P Mohanchandra, Y Lin, et al. Development of a high flow-rate/high operating frequency nitinol MEMS valve. *Proceeding of SPIE, Sensors and Smart Structures Technologies for Civil, Mechanical, and Aerospace Systems*, San Diego, California, March 09, 2008: 69322F.
25. Y T Ma, F R Kong, C L Pan, et al. Miniature tubular centrifugal piezoelectric pump utilizing wobbling motion. *Sensors and Actuators a-Physical*, 2010, 157(2): 322–327.
26. N N Rogacheva, C C Chung, S H Chang. Electromechanical analysis of a symmetric piezoelectric/elastic laminate structure: theory and experiment. *IEEE Trans Ultrason Ferroelectr Freq Control*, 1998, 45(2): 285–294.
27. Q F Cui, C L Liu, X F Zha. Study on a piezoelectric micropump for the controlled drug delivery system. *Microfluidics and Nanofluidics*, 2007, 3(4): 377–390.

Yu-Ting Ma, born in 1984, is currently an associate professor at *Suzhou Institute of Biomedical Engineering and Technology, Chinese Academy of Sciences*. She received her PhD degree from *University of Science and Technology of China* in 2011. Her research interests include piezoelectric actuators, piezoelectric pumps and ultrasonic motors. E-mail: mayt@sibet.ac.cn

Zhi-Guo Pei, born in 1986, is currently a research assistant at *Suzhou Institute of Biomedical Engineering and Technology, Chinese Academy of Sciences*. He received his master degree from *Huazhong University of Science and Technology, China*, in 2011. E-mail: peizg@sibet.ac.cn

Zhong-Xiang Chen, born in 1984, is currently a research assistant at *Suzhou Institute of Biomedical Engineering and Technology, Chinese Academy of Sciences*. He received his master degree from *Shanghai Institute of Technical Physics, Chinese Academy of Sciences*, China, in 2011. E-mail: chenxz@sibet.ac.cn